Generalized Method of Moments: A Novel Discretization Technique for Integral Equations

N. V. Nair, *Student Member, IEEE*, and B. Shanker, *Fellow, IEEE*

Abstract—**Typical method of moments solution of integral equations for electromagnetics relies on defining basis functions that are tightly coupled to the underlying tessellation. This limits the types of functions (or combinations thereof) that can be used for scattering analysis. In this paper, we introduce a framework that permits seamless inclusion of multiple functions within the approximation space. While the proposed scheme can be used in a mesh-less framework, the work presented herein focuses on implementing these ideas in an existing mesh topology. A number of results are presented that demonstrate approximation properties of this method, comparison of scattering data with other numerical and analytical methods and several advantages of the proposed method; including the low frequency stability of the resulting discrete system, its ability to mix different orders and types of basis functions and finally, its applicability to non-conformal tessellations.**

Index Terms—**Generalized method of moments, integral equations, low frequency stability, singular basis functions.**

I. INTRODUCTION

METHOD of moments (MoM) based solvers for integral equation formulations of electromagnetic problems have been in active use for over three decades [1]–[4]. Applications of MoM range from scattering and antenna analysis [5], [6] to electromagnetic compatibility [7] to photonics [8], etc. Typically, integral equations are solved by representing the unknown quantity (currents or fields) using a set of basis functions, testing the integral equation and solving the resulting discrete system. Basis functions are usually defined on a simplicial tessellation of the geometry. To date, basis functions used for vector electromagnetic formulations have been designed to invoke special properties across internal boundaries of the tessellation. Most popular in this category are the curl and divergence conforming basis functions. The former was introduced by Nedelec [9] *et al.* and implemented by Bossavit *et al.* [10], Barton *et al.* [11] and others. Divergence conforming functions were introduced by Raviart and Thomas [12] and Rao *et al.* [13]. Popularly called RWG functions, these form the basis for the construction of hierarchical higher order basis

functions [14], [15]. Both these basis functions are intimately related to the discretization of the geometry. This is required to maintain continuity of the various components across patch boundaries. A question has recently been posed whether the explicit enforcement of continuity should be required [16], [17]. Indeed [16] makes arguments that, in two dimensions, the use of a moderately high order complete basis function set eliminates the need for explicit enforcement of continuity conditions. Likewise it has been demonstrated in two dimensions, that the continuity constraints can be replaced by a partition of unity function to maintain the h and p convergence [18].

While advances have been made in the design of basis functions (both low and high order), the ability to include arbitrary functions in the basis space or to switch from one basis function to another is still limited. This may be critical when some information is known about the physics of the problem, and it is desirable to include this behavior in the definition of the basis functions. Higher order and singular variants of RWG functions have been suggested to partially alleviate this problem. For example, [19]–[21] incorporate Meixner series based functions in the basis space to model singular currents near edges. However, all of these techniques require careful design to handle the continuity of the various components of the basis functions across the internal boundaries of the tessellation. If the continuity constraints and the marriage with the tessellation could be removed, it would be possible to mix arbitrary classes of basis functions within the same geometric region. Unfortunately, all existing methods are specific to the underlying tessellation. Indeed, inclusion of a completely arbitrary basis function space might not even be possible within the framework of current basis function definitions. The need for a more general resolution to this problem motivates the work in this paper.

The problems of enlarging functions spaces has been addressed in the finite element community. Melenk *et al.* [22] developed the scalar GFEM as an umbrella framework for a class of mesh-based and mesh-less methods that allowed for the inclusion of a larger class of basis functions and demonstrated that the global errors were bounded by the local errors in approximation. The scheme was extended to vector finite elements for electromagnetics by Lu *et al.* [23]. The GFEM uses a product of a partition of unity function and a higher order approximation function to define basis functions on overlapping domains. However, extension of this method to integral equations is not trivial.

In GFEM, overlapping patches are defined by combining canonical patches. However, unlike in the GFEM framework, the patches for surface integral equations need to conform to an arbitrary scatterer surface and can not be expected to map

on to canonical geometries. This, in turn, makes the definition of *vector* basis functions on these non-canonical surfaces challenging. The structure of these patches may lead to functions that are piece-wise differentiable (for piecewise continuous patches). Therefore, computation of matrix elements involves evaluating singular and hyper singular integrals that need to be carefully handled. This paper addresses the resolution of these problems. A method of moments analogue of GFEM, called the generalized method of moments (GMM), is introduced in this paper.

Specifically, in this paper, we will address the following.

1) Describe a general framework for the definition of basis functions that is independent of the tessellation of the geometry on three dimensional bodies.
2) Design a mechanism for the construction of vector functions on arbitrary surfaces.
3) Describe a GMM implementation scheme for arbitrary geometries including:
   a) the design of overlapping patches conformal to the scatterer surface;
   b) the definition of functions on these non-canonical patches;
   c) the accurate computation of the matrix elements.
4) Present results that demonstrate several of the advantages of the GMM including:
   a) approximation of currents, its curl and divergence;
   b) computation of the radar scattering cross section data from topologically different structures;
   c) results obtained for polynomial mixed order and mixed function basis spaces;
   d) results of scattering from non-conformal discretization of scatterers;
   e) the ability to generate a low frequency stable scheme for the discretization of integral equations over a wide range of frequencies.

The rest of the paper is organized as follows. The problem is formally defined in Section II. Section III details the new discretization scheme and describes techniques for developing basis functions. Section IV discusses implementation issues and Section V provides a plethora of results to demonstrate the validity and utility of the proposed technique. Finally, Section VI summarizes the results and outlines future directions. A sketch of a modified rule for evaluation of some near-singular integrals is provided in Appendix A.

II. PRELIMINARIES

Consider a perfectly electric conducting body occupying a domain D_-. Let Ω denote the bounding surface of D_- and let the outward pointing unit vector normal at any point $\mathbf{r}$ on Ω be denoted by $\hat{\mathbf{n}}(\mathbf{r})$. Assume that a field $\{\mathbf{E}^i(\mathbf{r}), \mathbf{H}^i(\mathbf{r})\}$ is incident on this body and induces a current that radiates a scattered field $\{\mathbf{E}^s(\mathbf{r}), \mathbf{H}^s(\mathbf{r})\}$. The total electric and magnetic fields external to D_-, denoted by $\mathbf{E}(\mathbf{r})$ and $\mathbf{H}(\mathbf{r})$, can be decomposed into the incident and scattered fields by $\mathbf{E}(\mathbf{r}) = \mathbf{E}^i(\mathbf{r}) + \mathbf{E}^s(\mathbf{r})$, and $\mathbf{H}(\mathbf{r}) = \mathbf{H}^i(\mathbf{r}) + \mathbf{H}^s(\mathbf{r})$. The scattered fields can then be obtained using

$$\mathbf{E}^s(\mathbf{r}) = \mathcal{T} \circ \{\mathbf{J}(\mathbf{r})\} \doteq \frac{ik\eta_0}{4\pi} \int_\Omega d\mathbf{r}' g(R) \mathbf{J}(\mathbf{r}')$$
$$+ \frac{i\eta_0}{4\pi k} \int_\Omega d\mathbf{r}' \nabla\nabla g(R) \cdot \mathbf{J}(\mathbf{r}')$$
$$\hat{\mathbf{n}}(\mathbf{r}) \times \mathbf{H}^s(\mathbf{r}) = \mathcal{K} \circ \{\mathbf{J}(\mathbf{r})\}$$
$$\doteq \frac{1}{4\pi} \hat{\mathbf{n}}(\mathbf{r}) \times \int_\Omega d\mathbf{r}' \nabla g(R) \times \mathbf{J}(\mathbf{r}') \qquad (1)$$

where $g(R)$ is the Green's kernel for the Helmholtz equation, $R = |\mathbf{R}| = |\mathbf{r} - \mathbf{r}'|$, $\mathbf{J}(\mathbf{r})$ is the surface current defined by $\mathbf{J}(\mathbf{r}) = \hat{\mathbf{n}}(\mathbf{r}) \times \mathbf{H}(\mathbf{r})$, k is the wave number and η_0 is the intrinsic impedance of free space. An $e^{-i\omega t}$ time dependence is assumed and suppressed.

Combining (1) and the definitions of the total fields, the operator form of the electric and magnetic field integral equations (EFIE/MFIE) can be written as [3], [24]

$$\hat{\mathbf{n}}(\mathbf{r}) \times \hat{\mathbf{n}}(\mathbf{r}) \times \mathbf{E}^i(\mathbf{r}) = -\hat{\mathbf{n}}(\mathbf{r}) \times \hat{\mathbf{n}}(\mathbf{r}) \times \mathcal{T} \circ \{\mathbf{J}(\mathbf{r})\} \quad (2a)$$
$$\hat{\mathbf{n}}(\mathbf{r}) \times \mathbf{H}^i = (1/2 - \mathcal{K}) \circ \{\mathbf{J}(\mathbf{r})\}. \quad (2b)$$

As usual, a linear combination of EFIE and the MFIE results in the combined field integral equation (CFIE). Next, the GMM scheme used to solve for $\mathbf{J}(\mathbf{r})$ is described.

III. THE GENERALIZED METHOD OF MOMENTS

In order to remove the usually close knit relationship between the basis functions and the tessellation of the geometry, the GMM methodology offers the following approach to the solution of (2a) and (2b). The standard tessellation is replaced by (i) a set of overlapping patches that cover the domain Ω and (ii) a partition of unity subordinate to this cover. Basis functions are then defined on these partitions of unity and corresponding Galerkin testing yields a linear system of equations. In the rest of this section, we will discuss each of these steps in detail.

A. Partition of Unity Functions and Overlapping Patches

First, we define a covering $\{\Omega_i\}$ of the domain Ω. The patches Ω_i of the covering are allowed to overlap with each other and the covering itself satisfies a point-wise maximum overlap condition such that the number of patches overlapping any point is much less than the total number of patches. The actual design of these patches is nontrivial and will be discussed in Section IV. A partition of unity (PU) subordinate to $\{\Omega_i\}$ is then defined to satisfy the following properties:

Partition of Unity functions: Let $\{\psi_i\}$ be a sequence of functions defined on the cover $\{\Omega_i\}$ satisfying the following conditions:

i) $\text{supp}(\psi_i) \subset \Omega_i$ for all i;
ii) $\sum_i \psi_i \equiv 1$ on Ω;
iii) $|\psi_i(\mathbf{r})| \leq C_\infty \forall \mathbf{r} \in \mathbb{R}^3$;
iv) $|\nabla\psi_i(\mathbf{r})| \leq C_d = (C_\nabla)/(\text{diam}(\Omega_i)) \forall \mathbf{r} \in \mathbb{R}^3$.

Here C_∞ and C_∇ are two constants. Then $\{\psi_i\}$ is called an (M, C_∞, C_∇) PU subordinate to $\{\Omega_i\}$. The covering sets Ω_i will be referred to as patches and these patches take the place of the tessellation typically used in standard MoM. Note that while we have used nodes to define patches, the notion of patches can
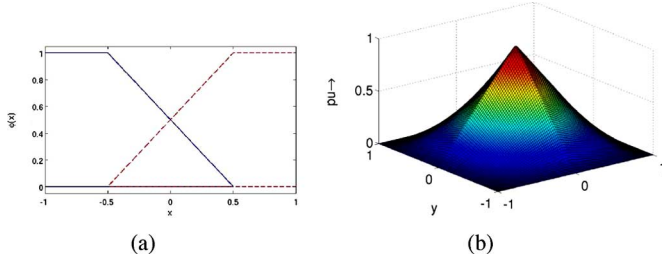
Fig. 1.   Examples of linear PU functions. (a) 1-D, (b) 2-D.

Fig. 2.   Construction of scalar GMM approximation and basis functions. (a) $\phi_i(\mathbf{x})$, (b) $j_i(\mathbf{x}) = \phi_i(\mathbf{x})\psi_i(\mathbf{x})$.

be more general. For instance, it can be based on edges. It follows that conventional MoM formulations can be thought of as special cases of GMM, with non-overlapping patches and a constant PU function. Conceptually, this is very much along the lines of comparing GFEM with other FEM formulations [25]. While this analogy is immediately apparent for scalar node-based formulations, one has to use different patch definitions (those based on edges) to realize mapping onto commonly used basis functions in computational electromagnetics. This concept of overlapping domains and corresponding PU functions is shown in Fig. 1(a). Generalization to higher dimensions can be effected using tensor products as shown in Fig. 1(b). Higher order extensions of these functions can be trivially defined [26]. Thus, by definition, the PU functions and overlapping domains ensures continuity across patch boundaries. The effects of this will be apparent in later numerical examples.

An overlapping PU based scheme was introduced by Bruno and others [27]–[31] to permit a higher order accurate integration scheme. As will be evident from the rest of the paper, the only thing that is in common is the use of overlapping PU framework. In all other aspects, the methodology introduced is completely different.

B. Definition of Basis Functions

Next, vector basis functions in each patch Ω_i are defined as a product of the PU function $\psi_i(\mathbf{r})$ and an appropriate approximation function of order m, $\boldsymbol{\nu}_i^m(\mathbf{r})$. For a GMM discretization, the approximation $\mathbf{J}_N$ to the current $\mathbf{J}$ can then be written as

$$\mathbf{J} \approx \mathbf{J}_N = \sum_{i=1}^{N} \mathbf{j}_i \doteq \sum_{i=1}^{N} \sum_m a_{i,m} \psi_i \boldsymbol{\nu}_i^m. \qquad (3)$$

Thus, the local approximating space on each patch Ω_i is defined as $\mathbf{V}_i \doteq \mathrm{span}_m\{\psi_i \boldsymbol{\nu}_i^m\}$. Note that within each patch Ω_i, there is no restriction on the set of functions $\boldsymbol{\nu}_i^m$. This set can be any mix of functions such as simple higher order complete polynomials, functions that best approximate the local physics, etc. The construction of a scalar basis function using a product of a two-dimensional linear PU function (shown in Fig. 1(b)) and a tensor product of higher order polynomials (in Fig. 2(a)) is shown in Fig. 2. For ease of presentation, the summation over m will be implicitly assumed and the corresponding indices will be dropped in the rest of this paper.

As is evident from the above discussion, the GMM provides a framework to include different approximation functions *without* explicitly requiring continuity constraints. The order of the PU function determines the order of continuity between patches
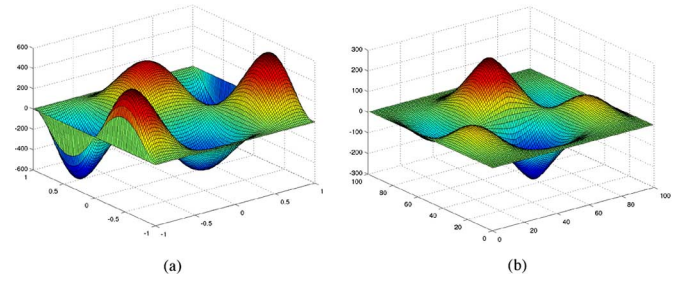
[25]. Thus, the global approximation inherits the smoothness of the PU function. An advantage offered by the GMM framework is the freedom of choice in the approximation function. By disassociating the definition of the approximation function from the underlying tessellation, GMM allows for the mixing of multiple types and orders of functions. Next, we develop vector approximation functions using a *local* quasi-Helmholtz decomposition of surface functions.

C. Design of the Vector Approximating Function

To define appropriate approximation functions $\boldsymbol{\nu}_i^m$ for the vector bases, we start with a surface Helmholtz decomposition of the current. For any vector field $\mathbf{J}(\mathbf{r})$ defined on the surface Ω, there exists two scalars fields $\phi(\mathbf{r})$ and $\zeta(\mathbf{r})$ such that

$$\mathbf{J}(\mathbf{r}) = \nabla_s \phi(\mathbf{r}) + \nabla_s \times \hat{\mathbf{n}}(\mathbf{r})\zeta(\mathbf{r}). \qquad (4)$$

Assume that we have an approximation $\boldsymbol{\nu}_i^m$ to the local behavior of the current $\mathbf{J}(\mathbf{r})$ on patch i. Then, define two sets of scalar functions $\phi_i^m(\mathbf{r})$ and $\zeta_i^m(\mathbf{r})$ such that

$$\boldsymbol{\nu}_i^{m,c} = \nabla_s \phi_i^m(\mathbf{r})$$
$$\boldsymbol{\nu}_i^{m,d} = \hat{\mathbf{n}}_i(\mathbf{r}) \times \nabla_s \zeta_i^m(\mathbf{r}) \qquad (5)$$

and consistent with (3) define the approximation to the current as

$$\mathbf{J}_N = \sum_{i=1}^{N} \sum_{q=\{c,d\}} \sum_m a_{i,q,m} \psi_i \boldsymbol{\nu}_i^{m,q}. \qquad (6)$$

Fig. 3(a) and (b) show the basis functions constructed using third order Legendre polynomials for $\phi_i^m(\mathbf{r})$ and $\zeta_i^m(\mathbf{r})$. These are obtained by multiplying the curl-free and divergence-free components of the approximation functions with the corresponding PU function for the patch. Note, however, that the local approximation is only quasi-curl and divergence free.

It is evident from the above exposition that there is no restriction on the functions ϕ_i^m and ζ_i^m. Indeed, if the local asymptotic behavior is known it can be readily incorporated into the approximation function space. Specifically, if the local behavior of current $(\mathbf{j}(\mathbf{r}) \approx \boldsymbol{\nu}_i(\mathbf{r}))$ is known to support at least one derivative, a possible way to compute the functions $\phi_i(\mathbf{r})$ and $\zeta_i(\mathbf{r})$ is given by the following lemma.

Lemma 3.1: Consider a vector function $\boldsymbol{\nu}_i(\mathbf{r})$ defined on Ω_i. Let ϕ_i and ζ_i be solutions to

$$\nabla^2 \phi_i(\mathbf{r}) = \nabla \cdot \boldsymbol{\nu}_i(\mathbf{r}) \qquad (7)$$
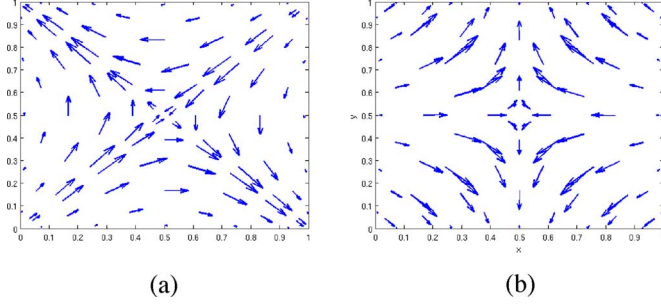
Fig. 3. Vector GMM basis functions. (a) $\psi_i \boldsymbol{\nu}_i^{m=3,q=c}$, (b) $\psi_i \boldsymbol{\nu}_i^{m=3,q=d}$.

$$\nabla^2 \zeta_i(\mathbf{r}) = \hat{\mathbf{n}}(\mathbf{r}) \cdot \nabla \times \boldsymbol{\nu}_i(\mathbf{r}) \tag{8}$$

then

$$\boldsymbol{\nu}_i = \nabla_s \phi_i(\mathbf{r}) + \nabla_s \times [\hat{\mathbf{n}}_i(\mathbf{r}) \zeta_i(\mathbf{r})]. \tag{9}$$

Scharstein [32] provides the proof of the above result along with some detailed insight into the physical implications of (7) and (8). We have previously shown for a class of surfaces, that once appropriate approximation and basis functions are defined the error propagated through the discretized integral operator is bounded above by the local error in approximation [33].

D. Benefits of the GMM Framework

The GMM method described in the previous subsections comprises of two components; (i) defining overlaps and partitions of unity and (ii) defining approximations functions in the partitions of unity. The definition of basis functions provides a mathematically rigorous framework for designing approximation spaces. From an intuitive perspective, we have always used the PU functions whenever the basis function space has comprised of pulses or hat functions for the analysis of scalar problems. Likewise, basis functions that are commonly used in the computational electromagnetics community (e.g., Rao-Wilton-Glisson [13], Buffa-Christiansen [34], characteristic basis [35] or Graglia-Wilton-Peterson [14]) can all be interpreted as a product of a partition of unity function and higher order approximating functions (with the correct definition of the PU domain). In most cases, the PU function is implicitly assumed and is typically a pulse function. When it is a pulse function, one has to worry about means to achieve conformal behavior between neighboring elements. As in GFEM [25], the use of basis functions that explicitly comprise of a product of an overlapping partition of unity and approximating functions removes the need for such boundary treatment between different sub domains, and dramatically increases the number of functions that can be used for approximation. For instance, one can use a third order approximation in a domain next to one where a first order is being used, without explicitly enforcing any condition. Or for that matter, mixture of polynomial and non-polynomial basis functions. Use of the these definitions of basis will be demonstrated in the Section V. In the next Section, we present specifics of the implementation of the general GMM scheme for arbitrary 3D scatterers.

IV. IMPLEMENTATION OF THE GMM

While the development of basis functions in previous Section is general and can be applied to arbitrary patch definitions, such as those described in [29], or within a "meshless" environment, we would like to also develop additional mechanism for using this with existing and readily available mesh generators. Thus, in what follows, we present a scheme to generate patches, define basis functions and compute matrix elements on an underling mesh topology. It is assumed that a triangular tessellation of the geometry is available. Extension of this scheme to higher order tessellations is relatively straightforward.

A. Construction of Overlapping Patches

To define a set of overlapping patches starting from a triangular mesh, we designate each node as the "center" of a patch, defined as the union of all triangles that share the node.

a) Overlapping Patches: Consider a set of nodes $\mathcal{N}_L = \sum_{i=1}^{L} \{\mathcal{N}_i\}$ and a corresponding triangulation $\Delta_N = \sum_{n=1}^{N} \{\Delta_n\}$ of a domain Ω. Let $\{\mathcal{N}_{n_{j=1-3}}\}$ be the set of nodes associated with triangle Δ_n. For each node $\mathcal{N}_i$, denote a corresponding patch Ω_i defined by a set of triangles; $\Omega_i = \{\Delta_n : \Delta_n \in \Delta_N, \mathcal{N}_\rangle \in \mathcal{N}_{n_j}\}$. The GMM covering is defined as the set of these (overlapping) patches $\{\Omega_i\}$. The overlap between any two patches Ω_p and Ω_q is another set of triangles $\Delta_{p,q} \doteq \Omega_p \cap \Omega_q$.

This definition of GMM patches from a union of polygonal shapes can also be seamlessly translated to higher order geometries defined on triangulations described in [14]. In the remainder of this section, Δ_n will be used to represent both flat and equivalent higher order triangulations of the surface. The above patch design also allows for integration on the triangles described by the original tessellations and therefore, allows the use of available integration rules.

The next step is to develop a consistent definition for basis functions on these patches. Note that these patches are no longer coplanar and do not correspond to any canonical geometry (unlike triangles, quads, etc.). This necessitates the careful definition of functions on Ω_i so as to maintain continuity. To this end, we define a projection plane for each patch.

b) Patch Normal and Projection Plane: Consider a patch Ω_i composed of m triangles $\Omega_i = \bigcup_{k=1}^{m} \{\Delta_k\}$. Next, define an average normal for the patch, $\hat{\mathbf{n}}_i$ as $\hat{\mathbf{n}}_{i,\varepsilon} = 1/m \sum_{k=1}^{m} \hat{\mathbf{n}}(\mathbf{r}_k)$, where $\mathbf{r}_m$ are points chosen on each of the triangles that make the patch such that $\mathbf{r}_m \subset \Omega_i \cap \Delta_k$ and $\|\mathbf{r}_k - \mathbf{r}_i\|_2 \leq \varepsilon$. The projection plane for patch Ω_i, $\mathcal{P}_i$ is defined as the plane passing through $\mathbf{r}_i$ and normal to $\hat{\mathbf{n}}_i$. For purposes of illustration, Fig. 4 shows the construction of one patch and its corresponding projection plane. Observe that the differences between the patch normal $\hat{\mathbf{n}}_i$ and the normals of the individual member triangles provide an intuitive measure of the "sharpness" of the surface at $\mathbf{r}_i$. This information can be used as a criteria for the design of approximation functions. If the surface is discontinuous, it is partitioned into areas that are piecewise continuous and then the above procedure is applied to each portion.

Once the normal and the projection planes are defined for each patch, basis functions are defined on the projection of the
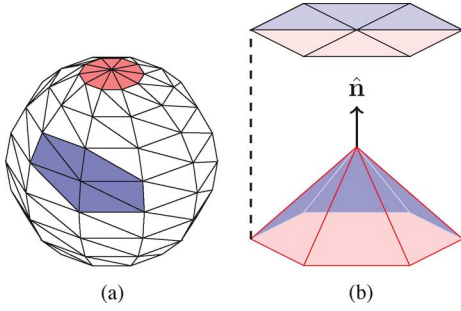
Fig. 4. Construction of (a) GMM Patches (Ω_i) shown as shaded region and (b) projection planes (Γ_i) from standard triangulations. (a) Definition of GMM Patch Ω_i, (b) construction of projection plane Γ_i.

Fig. 5. Basis functions defined on (a) the projection plane and (b) the true geometry (surface of a tessellated sphere).

entire patch on the plane using a local coordinate system on the projection plane.

c) Local Coordinate System: Let Γ_i be the projection of a patch Ω_i on $\mathcal{P}_i$. For the rest of the discussion, primed coordinates denote the projection of the corresponding global coordinate on $\mathcal{P}_i$ (note that, by construction, $\mathbf{r}_i = \mathbf{r}'_i$). Two local projection vectors are generated for each patch $\hat{\mathbf{u}}_{p,i}(\mathbf{r}')$ and $\hat{\mathbf{v}}_{p,i}(\mathbf{r}')$ as $\hat{u}_p \doteq \mathbf{u}_p/\|\mathbf{u}_p\|_2$ where $\mathbf{u}_p = \mathbf{r}' - \mathbf{r}'_i$ such that $\|\mathbf{u}_p\|_2 \geq \|\mathbf{r} - \mathbf{r}'_i\|_2 \forall \mathbf{r} \in \Gamma_i$ and $\hat{\mathbf{v}}_p = \hat{\mathbf{n}}_i \times \hat{\mathbf{u}}_p$.

With this preamble, it is now possible to define a mapping from regular x, y, z coordinate space into the u, v coordinate space defined on the projection Γ_i as follows:

- $\forall \mathbf{r} \in \Omega_i \exists \mathbf{r}' \in \Gamma_i$;
- define $u = \mathbf{r}' \cdot \hat{\mathbf{u}}_p$ and $v = \mathbf{r}' \cdot \hat{\mathbf{v}}_p$;
- then the local coordinates $\mathbf{u}$ and $\mathbf{v}$ are given by $u\hat{\mathbf{u}}_p$ and $v\hat{\mathbf{v}}_p$.

Approximation and basis functions are now constructed by defining functions on the corresponding planar coordinates. One consequence of the choice of the coordinate system is that the projection coordinates span an area that *contains, but is not limited to*, Γ_i. This is, however, implicitly handled by the definition of the PU functions. Since the PU functions decay to zero on at the boundary of the patch, the basis function will also be compactly supported within the patch.

Given the definitions above, it is important to ensure that functions that are continuous in the projection domain are so in the real space as well. The following theorem (stated without proof) prescribes the necessary conditions.

Theorem 4.1: Given a surface description $\Omega_i(\mathbf{r})$ that is at least $C^1(\mathbb{R}^3)$ smooth, consider any function $F(u(\mathbf{r}), v(\mathbf{r}))$ defined on the projection Γ_i. Then, if $F \in C^m(\Gamma_i)$ then $F \in C^m(\Omega_i)$ for any m.

The proof follows from the definition of partial derivatives. While a corresponding result does not hold for piecewise continuous triangulations, in practice we have observed that it is possible to construct functions that are continuous across the interior edges of the patch. This fact is shown in Fig. 5 where a set of polynomial functions are defined on a flat projection plane, in Fig. 5(a), and then transformed to a non-flat, piecewise linear, triangulation in Fig. 5(b). It is apparent from the figures that there are no discontinuities introduced due to the projection.
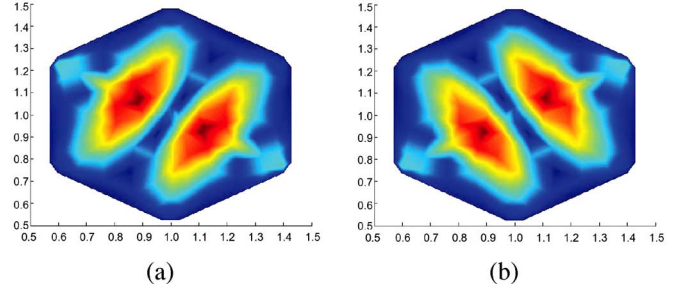
B. Computation of Matrix Elements

Next, the discrete versions of the EFIE and the MFIE are constructed using Galerkin testing. It can be verified that the computation of the matrix elements involves the evaluation of the following three types of integrals:

$$\int_{\Omega_i} d\mathbf{r} \mathbf{t}(\mathbf{r}) \cdot \int_{\Omega_j} d\mathbf{r}' g(R) \mathbf{j}(\mathbf{r}') \tag{10}$$

$$\int_{\Omega_i} d\mathbf{r} \mathbf{t}(\mathbf{r}) \cdot \hat{\mathbf{n}}(\mathbf{r}) \times \int_{\Omega_j} d\mathbf{r}' \nabla g(R) \times \mathbf{j}(\mathbf{r}') \tag{11}$$

$$\int_{\Omega_i} d\mathbf{r} \mathbf{t}(\mathbf{r}) \cdot \int_{\Omega_j} d\mathbf{r}' \nabla \nabla g(R) \cdot \mathbf{j}(\mathbf{r}') \tag{12}$$

for $\mathbf{r} \in \Omega_i$ and $\mathbf{r}' \in \Omega_j$.

It is well known that (10) has an integrable singularity that can be numerically handled using either singularity cancellation [36], [37] or singularity evaluation [38] schemes. In our implementation, we use the method developed in [38] that is extensible to higher order geometries, near singular terms and is also independent of the basis function definition.

The integral involved in (11) contains a hyper-singular term. However, the complete integral is well behaved and its handling is well documented in literature. The only departure we make from standard practice is the use of a singularity subtraction scheme near the $\mathbf{r} = \mathbf{r}'$ using a technique based on the scheme outlined in [39] for near singular terms.

The evaluation of (12) is more involved. Assume that $\Omega_{i(j)}$ is the union of a set of triangles denoted by $\cup \Delta_{i(j)}$. Then (12) can be rewritten in either of the following two forms:

$$\int_{\Omega_i} d\mathbf{r} \mathbf{t}(\mathbf{r}) \cdot \int_{\Omega_j} d\mathbf{r}' \nabla \nabla g(R) \cdot \mathbf{j}(\mathbf{r}')$$

$$= \int_{\cup \Delta_i} d\mathbf{r} \mathbf{t}(\mathbf{r}) \cdot \int_{\cup \Delta_j} d\mathbf{r}' \nabla \nabla g(R) \cdot \mathbf{j}(\mathbf{r}')$$

$$= -\int_{\cup \Delta_i} d\mathbf{r} \nabla_s \cdot \mathbf{t}(\mathbf{r}) \int_{\cup \Delta_j} d\mathbf{r}' \nabla_s g(R) \cdot \mathbf{j}(\mathbf{r}')$$

$$+ \int_{\cup \partial \Delta_i} d\mathbf{r} \hat{\mathbf{m}}_i(\mathbf{r}) \cdot \mathbf{t}(\mathbf{r}) \int_{\cup \Delta_j} d\mathbf{r}' \nabla_s g(R) \cdot \mathbf{j}(\mathbf{r}') \tag{13a}$$

or

$$= -\int_{\cup \Delta_i} d\mathbf{r} \nabla_s \cdot \mathbf{t}(\mathbf{r}) \int_{\cup \Delta_j} d\mathbf{r}' g(R) \nabla'_s \cdot \mathbf{j}(\mathbf{r}')$$

$$+ \int_{\cup \partial \Delta_i} d\mathbf{r} \hat{\mathbf{m}}_i(\mathbf{r}) \cdot \mathbf{t}(\mathbf{r}) \int_{\cup \Delta_j} d\mathbf{r}' g(R) \nabla'_s \cdot \mathbf{j}(\mathbf{r}')$$

$$- \int_{\cup \partial \Delta_i} \mathrm{dr} \hat{\mathbf{m}}_i(\mathbf{r}) \cdot \mathbf{t}(\mathbf{r}) \int_{\cup \partial' \Delta_j} \mathrm{dr}' g(R) \hat{\mathbf{m}}_j(\mathbf{r}') \cdot \mathbf{j}(\mathbf{r}')$$

$$+ \int_{\cup \Delta_i} \mathrm{dr} \nabla_s \cdot \mathbf{t}(\mathbf{r}) \int_{\cup \partial' \Delta_j} \mathrm{dr}' g(R) \hat{\mathbf{m}}_j(\mathbf{r}') \cdot \mathbf{j}(\mathbf{r}') \quad (13b)$$

where $\hat{\mathbf{m}}_i$ and $\hat{\mathbf{m}}_j$ are the unit normals to each boundary $\partial \Delta_i$ and $\partial' \Delta_j$ of Δ_i and Δ_j, respectively. The divergence operator $(\nabla^{(\prime)})$ can be reduced to the corresponding surface divergence operator $(\nabla_s^{(\prime)})$ because $\mathbf{j}(\mathbf{r})(\mathbf{t}(\mathbf{r}))$ are surface functions. Since the set of triangles forming a patch are not co-planar, the normal $\mathbf{m}_{i(j)}$ is not continuous within a patch. Therefore, the integrals on either side of an edge do not cancel. Thus, we need to compute all the terms on the right-hand side of the expansion. One saving grace is that the integral vanishes (as a consequence of the PU function) on the outer boundary of the patch and thus only interior triangle edges need to be considered. It is clear that (13a) involves integrals that are an order of singularity higher than (13b). However, as $\mathbf{r} \to \mathbf{r}'$ (g is singular), (13b) can no longer be used since $(1/R)$ is not integrable on a line when $\mathbf{r} \to \mathbf{r}'$. As a result, in the GMM implementation, we split the integral in (12) into the following categories.

1) $\mathbf{r}$ and $\mathbf{r}'$ Lie on the Same Triangle: In this case, we can utilize the singularity subtraction technique outlined in [40] to extract and compute the integral. This technique is stable for linear patches but extension to higher order geometry discretizations requires some additional work.

2) $\mathbf{r}$ and $\mathbf{r}'$ Lie on Triangles That Share an Edge: In this case, the integral is not singular but the $1/R^3$ term needs to be handled carefully. This case is evaluated using (13a). The line integral exists in this case since the inner (source) integral is on the surface and the outer (testing) integral is on the line and $\nexists \mathbf{r} \in \partial \Delta_i$ and $\mathbf{r}' \in \Delta_j \cdot \ni \cdot \mathbf{r} = \mathbf{r}'$. The first term in the expansion can be computed for near singular (but non-singular) terms using a modification of the method described in [38]. The transformation in [38] has been modified slightly to integrate terms of the type $(1/R^2)$. A brief exposition can be found in Appendix A.

3) $\mathbf{r}$ and $\mathbf{r}'$ Are Not in Neighboring Triangles But Are Close $(|\mathbf{r} - \mathbf{r}'| \leq 0.15\lambda)$: Here we use (13b) to evaluate the integral due to the (now) better behaved nature of the singularity.

4) $\mathbf{r}$ and $\mathbf{r}'$ Are Sufficiently Separated From Each Other: In this case, the singularity is no longer a concern and the integral can be evaluated using either of the two expressions above, using standard numerical quadrature.

C. Integration With Acceleration Techniques

Once the basis functions are defined and the appropriate integration rules chosen, integration with the wideband fast multipole method (FMM) is straightforward [41]–[43]. This code has been augmented with this flavor of wideband FMM using the methodology described in the [43] and will not be further elucidated here.

V. Results

Next, via a series of numerical experiments, we will demonstrate that the discretization framework proposed in this paper (i) provides excellent approximation of the unknown currents and its derivatives and (ii) accurate results for scattering from several topologically different objects, (iii) demonstrate the viability of this method to accurately analyze scattering from objects using a mixture of basis functions, (iv) demonstrate analysis from objects meshed with non-conformal meshes and (v) low frequency stability the choice of basis. Where necessary, results have been obtained using a GMM code augmented by FMM.

A. Quality of Approximation

The first goal is to test whether multiple functions can be seamlessly mixed together within the GMM approximation space. This will be verified by a series of numerical experiments described next. It is assumed that the current in a domain Ω satisfies some prescribed functional dependence $\mathbf{J}(\mathbf{r}) = \mathbf{f}(\mathbf{r})$, and is approximated using basis functions as

$$\mathbf{J}_N(\mathbf{r}) = \sum_i a_i \mathbf{j}_i(\mathbf{r}) = \sum_{i=1}^{N} \sum_{q=d,c} \sum_m a_{i,m} \psi_i \boldsymbol{\nu}_{i,q}^m(\mathbf{r}). \quad (14)$$

The coefficients of these basis functions are computed by solving a discrete system

$$\bar{\bar{\mathbf{Z}}} \bar{a} = \bar{b} \quad (15)$$

where $\mathbf{Z}_{i,j} = \langle \mathbf{j}_i, \mathbf{j}_j \rangle$ and $\mathbf{b}_i = \langle \mathbf{j}_i, \mathbf{J} \rangle$ The approximation error is defined as

$$\varepsilon(\mathbf{r}) = \frac{\left| \mathbf{f}(\mathbf{r}) - \sum_{i=1}^{N} a_i \mathbf{j}_i \right|}{|\mathbf{f}(\mathbf{r})|} \quad (16)$$

and is computed by oversampling the currents on the geometry. Error in using this approximation to compute the curl and divergence of the current is found in a similar manner.

For each test described next, the approximation was computed on a square domain of side 1.0 m using overlapping patches, each of size $h = 0.2$ m. Fig. 6(a)–(b) show the convergence of the maximum approximation error with approximation order p for each of the tests.

1) Approximation of Polynomial Functions: It was earlier argued that the GMM scheme permits the mixing of basis functions of various types. For this to be effective, it is important that the higher order functions do not corrupt the approximation of smooth functions. Fig. 6(a) shows the convergence of the approximation error for two functions (i) a constant $\mathbf{f}(\mathbf{r}) = \hat{\mathbf{x}}$ and (ii) a polynomial $\mathbf{f}(\mathbf{r}) = \hat{\mathbf{x}} y^3 + \hat{\mathbf{y}} x^3$. As expected, the error is consistently less than 10^{-12} for the constant function. Similarly, it is very interesting to note here that once the order of the approximation reaches the order of the polynomial function $(p = 3)$, the error in the GMM scheme drops to machine precision.

2) Approximation of Sinusoidal Functions: Fig. 6(b) shows the convergence graphs for $\mathbf{f}(\mathbf{r}) = \hat{\mathbf{x}} \sin(x) \sin(y)$ and $\mathbf{f}(\mathbf{r}) = \hat{\mathbf{x}} \exp(-\mathbf{j}\mathbf{k} \cdot \mathbf{r})$. The figures show the convergence curve for both the approximation in the current and its curl and divergence. As seen in the figures, the error in both $\nabla \cdot \mathbf{J}$ and $\nabla \times \mathbf{J}$ is the same and of order $(p - 1)$, as expected.

3) Approximation of Non-Smooth and Near-Singular Functions: The true power of the partition of unity comes into play when the functions are discontinuous across the patch boundaries. To demonstrate this, consider a function that is first order
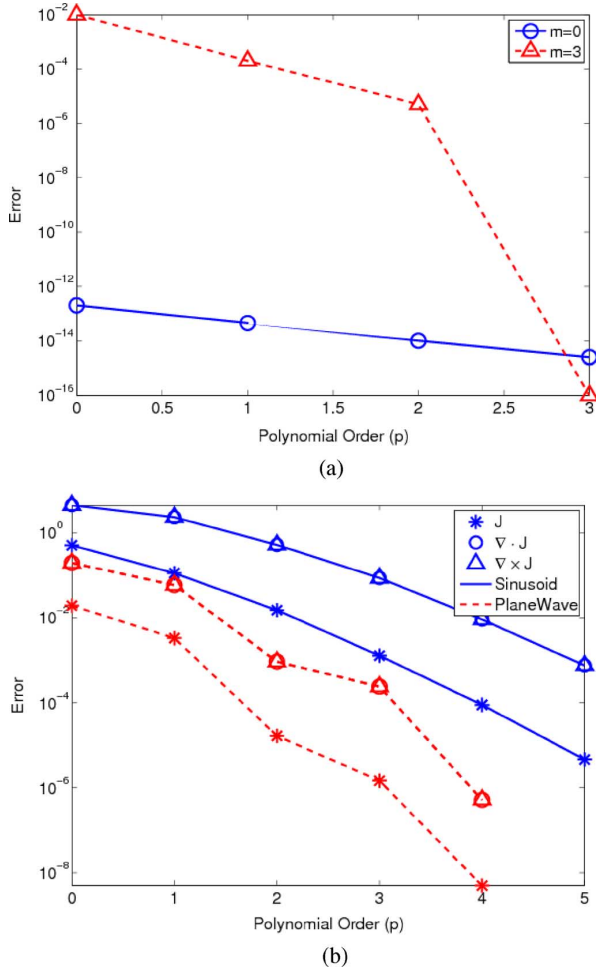
(a)

(b)

Fig. 6. Quality of approximation of (a) polynomial and (b) sinusoidal functions. (a) $\mathbf{f}(\mathbf{r}) = \hat{\mathbf{x}}(m = 0)$ and $\mathbf{f}(\mathbf{r}) = \hat{\mathbf{x}}y^3 + \hat{\mathbf{y}}x^3(m = 3)$, (b) $\mathbf{f}(\mathbf{r}) = \hat{\mathbf{x}}\sin(x)\sin(y)$ and $\mathbf{f}(\mathbf{r}) = \hat{\mathbf{x}}\exp(-\mathbf{j}\mathbf{k}\cdot\mathbf{r})$.

(a)

(b)

Fig. 7. Quality of approximation of discontinuous function. (a) Error without PU, (b) error with PU.

discontinuous on a line that does not coincide with the patch boundary described by

$$\mathbf{f}(\mathbf{r}) = \begin{cases} \hat{x} & \forall x \leq x_0 \\ \hat{x}x/x0 & \forall x \geq x_0 \end{cases}. \tag{17}$$

Fig. 7(a) shows the approximation error obtained by using two separate functions in each patch without overlapping patches or a partition of unity. As can be clearly seen, the error in the function propagates through the patch because the discontinuity does not coincide with the patch boundary. Fig. 7(b) on the other hand, shows the same function approximated by overlapping patches and a partition of unity. As the figures clearly show, the error is significantly better in the GMM basis function framework.

Next, we examine the efficacy of using a GMM framework in approximating currents near a one dimensional edge up to a distance 1 m from the tip; see [19], [20] and references therein for details of some of the basis functions in current use. Typically, the current perpendicular to a one-dimensional edge is modeled using leading order terms from a Meixner series expansion (as $1/\sqrt{d}$ where d is the distance from the edge). This functional
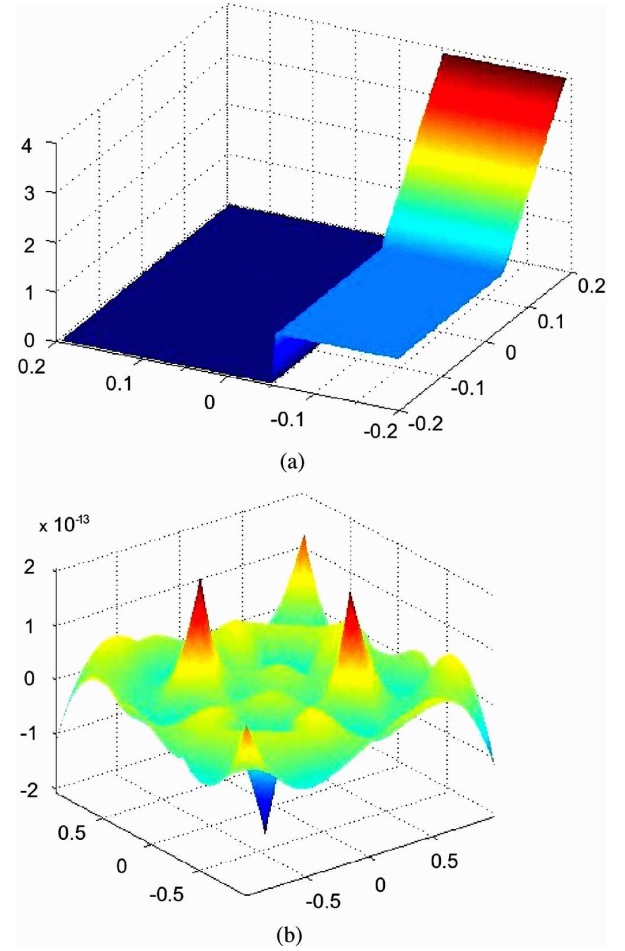
dependence is shown in Fig. 8. This problem has been studied in [19] where the dependence is incorporated by changing the basis function in the patch near the edge. Specifically, in [19] the domain is partitioned into segments of size h; in the patch nearest the edge, the basis function is chosen to be the leading term of the Meixner series, and in all other patches it is either a pulse or a hat function. In the following example, we will examine the error in representation of this function using basis functions within and without a partition of unity framework.

Fig. 9 shows three error curves, the first is obtained using the basis functions in [19]. In this case, the basis function in the first patch is $1\sqrt{d}$ where d is the distance from the edge/tip. Starting from the second patch onwards hat functions are used as basis. This result establishes a baseline for comparison of convergence. The second curve is obtained using basis functions that are a combination both singular functions and higher order polynomials. Specifically, patches comprise of two adjacent segments. On patches that lie within a perpendicular distance of 0.1 m of the edge, it is assumed that basis functions are a superposition of singular functions of the form $1/\sqrt{d}$ where d is the distance from the origin and polynomials that are complete to order $p = 2$. As is evident from Fig. 9, this class of basis functions provides better approximating properties. The third curve
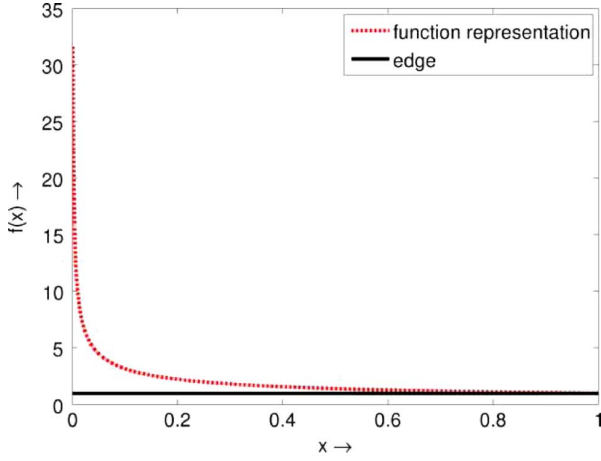
Fig. 8. Functional representation of a current near an edge. The solid line denotes the 1-D edge while the dashed line shows the leading term of the Meixner series approximation to the current.
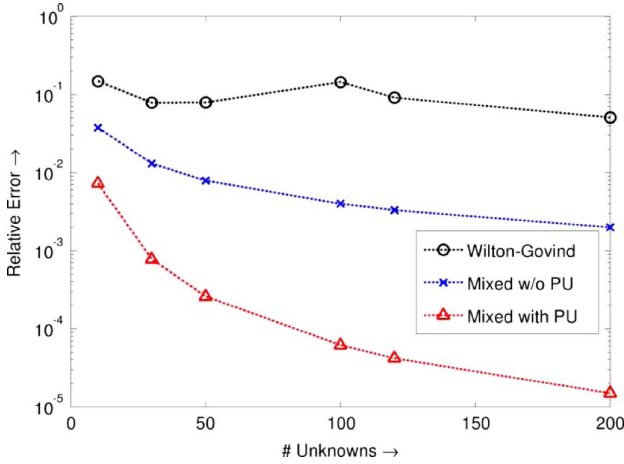

Fig. 9. Comparison of approximation error with and without PU.

in Fig. 9 demonstrates the convergence obtained by using a partition of unity function. As before, patches are defined to comprise of two adjacent segments. For all patches whose perpendicular distance is less than 0.1 m from the edge, basis functions comprise of a linear combination of singular functions $(1/\sqrt{d})$ and polynomials complete to $p = 1$, both of which multiplied by a linear PU function. For all patches that are further from this point, the basis function is a product of a linear PU function and a polynomial of order $p = 1$. The use of a lower order polynomial ensures that the order of the basis function is $p = 2$. As is evident, the approximation provided by this scheme is considerably better than the previous case. In large part, this result is due to better continuity properties offered by the PU function; proofs for convergence of approximation to scalar and vector functions have been provided in [22], [23].

As can be seen from all the examples presented in this Section, for a series of discretizations, the PU-based approximation consistently performs well. To a large extent, this is a consequence of the GMM framework which decouples the traditional link between tessellation and the basis function definition. In

other words, it is possible to define dramatically different basis functions in the same patch (or adjacent patches) without worrying about auxiliary conditions to maintain continuity. Continuity of these functions is provided by the partition of unity function. As a result, the quality of approximation is better. In the next Section, we further explore the capabilities of this representation by applying it to compute electromagnetic scattering.

B. Scattering Results

In this section, we compare the radar cross-section from a variety of PEC objects. Unless otherwise noted, in all examples that follow, the incident field is assumed to be $\hat{x}$ polarized and propagating along the $-\hat{z}$ direction. The object is discretized using a triangulation such that the average edge length is 0.1λ and GMM patches are constructed using the scheme outlined in this paper. Since the GMM patches are of arbitrary shape, we define the side of the smallest enclosing cube for each GMM patch as an equivalent "edge length" (h). In the following examples, h varies from 0.1λ to 0.4λ, where λ is the wavelength of the incident field. Unless specified otherwise, the GMM approximation functions, ϕ_i^m and ζ_i^m, were constructed using Legendre polynomial functions complete to order p. Finally, note that the underlying triangulation used is the same for both GMM and RWG or its higher order variant. In what follows, we have used the notation "higher order RWG" to denote basis functions develop by Graglia, Wilton and Peterson [14].

1) Analytical Validation and p-Convergence: Fig. 10(a) compares the RCS of a PEC sphere obtained using GMM against analytical solutions evaluated using a Mie-series representation. The number of GMM unknowns (N_{GMM}) used is 200, 776 and 3080 for spheres of radii $0.2\lambda, 0.6\lambda$ and 1.0λ respectively. As is evident, the agreement between the two is excellent. Fig. 10(b) compares the convergence of the error as a function of the polynomial order of the basis function used, for both the GMM and higher order RWG [14]. The comparison is performed for backscattered data obtained from two scatterers (i) a sphere of diameter 1.0λ and (ii) a NASA almond that fits in a box of dimensions $0.4\lambda \times 1.15\lambda \times 3\lambda$. The number of unknowns for the sphere is as follows: $N_{\text{GMM}} = 964, 2604$ and 5208 for $p = 1, 2, 3$, respectively. The number of higher order RWG unknowns are $N_{\text{RWG}} = 4230, 9072, 15552$ at $p = 1, 2$ and 3, respectively. For the almond, $N_{\text{GMM}} = 948, 4656$ and 7560 at $p = 2, 3$ and 4, respectively and $N_{\text{RWG}} = 3800, 7980$ and 13680 at $p = 2, 3$ and 4, respectively. In all cases, the incident field was $\hat{x}$ polarized and incident along $\hat{z}$. The axis of the almond was oriented along $\hat{x}$. The convergence is evaluated for the error between the numerical and analytical solution for the sphere and for the relative error between successive steps in the case of the almond. In each case, the approximation functions used for GMM were p-order complete polynomials in each of the local projection co-ordinate spaces. Correspondingly the basis functions used for higher order RWG were of the type suggested in [14] and are complete to order p. The exponential nature of the convergence is clearly evident from the figure. It is interesting to note that the convergence rate for the GMM scheme seems consistently better than that for RWG for both the geometries.
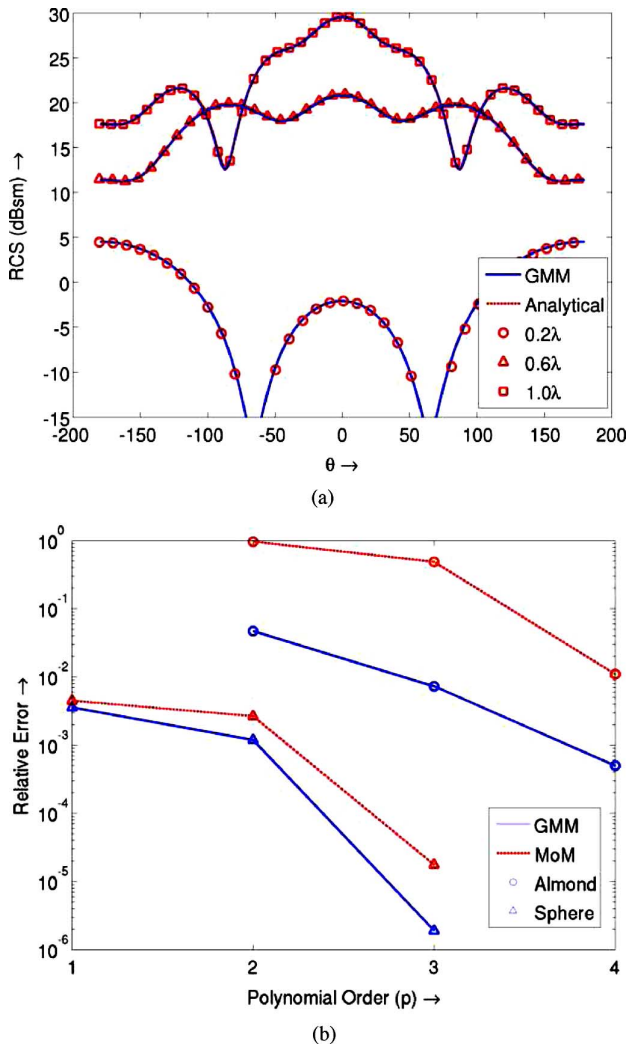
Fig. 10.   Validation Studies. (a) Comparison with analytical solution for PEC sphere of various radii, (b) convergence with polynomial order (Sphere and NASA Almond).

Fig. 11.   RCS comparisons—GMM vs. traditional RWG. (a) Plate ($\lambda \times \lambda$) and Open cavity ($\lambda \times \lambda \times \lambda$) (using EFIE), (b) Sphere (λ), Conesphere ($2.6\lambda \times 0.5\lambda$) and NASA Almond (1:3:9) (using CFIE).

2) Comparison With Standard RWG: In this section, the RCS obtained due to scattering from a variety of geometries is computed using the GMM basis functions and compared against that obtained using RWG basis functions. In all cases, first order complete polynomials were used to construct basis functions for the GMM. Similarly first order RWG functions were used for the RWG scheme.

Fig. 11(a) shows the RCS from a square PEC plate of side λ discretized using 248 effective GMM unknowns (N_{GMM}) and 228 RWG unknowns (N_{RWG}); and an open cavity of dimensions $\lambda \times \lambda \times \lambda$ ($N_{\text{GMM}} = 402, N_{\text{RWG}} = 1746$). The incident field is $\hat{\mathbf{x}}$ polarized and propagates along $\hat{\mathbf{z}}$. The RCS is computed by an EFIE formulation discretized using both the GMM and a standard RWG. It is evident that the GMM result agrees very well with the standard RWG formulation.

Figs. 11(b) compares the RCS obtained due to scattering from a sphere of radius 1.0λ ($N_{\text{GMM}} = 1736, N_{\text{RWG}} = 4320$), an EMC benchmark cone-sphere of height 2.6λ and radius 0.5λ ($N_{\text{GMM}} = 1792, N_{\text{RWG}} = 1656$) and a NASA almond that fits in a box of dimensions $0.4\lambda \times 1.15\lambda \times 3\lambda$ (1:3:9) ($N_{\text{GMM}} =$
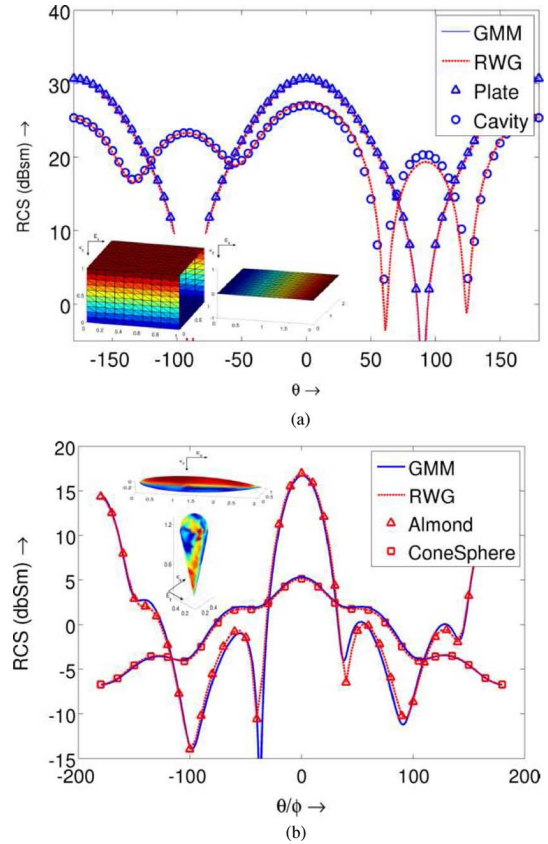
$1528, N_{\text{RWG}} = 2800$). The cone-sphere and the almond are both oriented with their long axis along $\hat{\mathbf{x}}$. In each case, the incident field is $\hat{\mathbf{x}}$ polarized and propagates along the $\hat{\mathbf{z}}$ direction. Both the GMM and the MoM results are computed using a CFIE. While the sphere and cone-sphere results are obtained using polynomials of order $p = 1$, the almond results are obtained for both $p = 1$ and $p = 2$. As is evident from the figures, the agreement between the GMM and MoM is excellent.

3) Comparison With Measured Data: Finally, we consider scattering from a PEC cube of side 0.7λ. The cube was discretized using $N_{\text{GMM}} = 320$ and $N_{\text{RWG}} = 1500$ unknowns. Measured data has been reported for scattering from this structure in [44]. Again, electric field polarized along $\hat{\mathbf{x}}$ is assumed in the $\hat{\mathbf{z}}$ direction. Fig. 12 shows the comparison of RCS obtained by GMM and RWG against that obtained from experimental measurement. Again, there is excellent agreement between all three RCS data sets. These numerical experiments demonstrate the ability of the GMM technique to accurately use first and higher order polynomial basis functions to compute scattering cross-sections from a wide variety of geometries.

C. Flexibility of the GMM Scheme

The results presented thus far demonstrate the approximation quality of GMM basis functions, the convergence characteristics and applicability to calculating scattered fields from a variety of topologically different objects. In addition, the GMM scheme
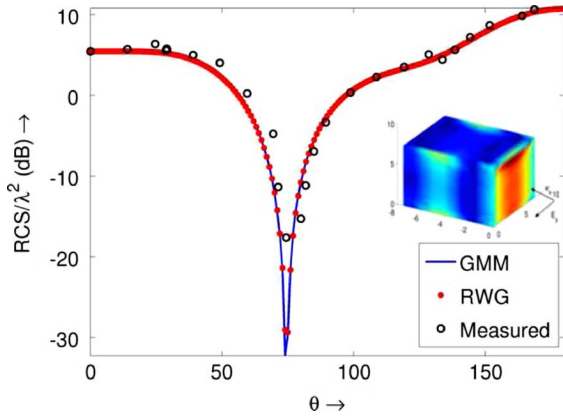
Fig. 12. RCS comparison for a PEC box (0.7λ) GMM vs. RWG vs. measured data.

also provides the flexibility to mix different types of orders and types of basis functions, and use non-conformal meshes with minimal change to the overall computational structure. The examples presented in this section demonstrate these advantages. In all cases analyzed in this section, the incident field is polarized along the $\hat{x}$ direction and the field is incident along the $-\hat{z}$ direction.

1) Mixing Orders of Basis Functions: First, consider a PEC box of dimensions $\lambda \times 4\lambda \times \lambda$ that is oriented along the $\hat{\mathbf{x}}$ direction. This box is meshed at 0.1λ everywhere to obtain an initial triangulation. GMM patches and basis functions complete to order $p = 1$ are constructed to obtain the RCS due to illumination by a $\hat{z}$ directed incident electric field polarized along $\hat{E}_x$. Next, the same geometry is discretized using an edge length 0.25λ for $0.75\lambda \leq \mathbf{x} \leq 2.25\lambda$ and of edge length 0.1λ elsewhere. Basis functions of order $p = 2$ are used in the larger patches while basis functions of order $p = 1$ are used in the small patches. RCS computed using this configuration is then compared against that obtained earlier using a denser (almost) uniform discretization in Fig. 13(a). As is evident, the agreement is excellent. While the agreement between the two RCS data sets demonstrates the ability of the technique to mix different orders of basis functions, the ease with which this mixing can be effected within the GMM scheme is equally important. In our implementation, types and orders of basis functions to be used in a patch are specified by an input flag. This level of flexibility in choice of basis functions is unique to the GMM scheme.

Fig. 13(b) demonstrates two RCS obtained due to scattering from a PEC almond that fits in a box of size $0.3\lambda \times \lambda \times 3.2\lambda$. The first RCS is obtained using basis functions of order $p = 1$ everywhere and then second is obtained using basis functions of order $p = 2$ in all patches within 0.2λ of the tip and $p = 1$ everywhere else. Again, the agreement of between the two RCS data is excellent and demonstrates the ability of the GMM technique to mix different basis functions.

Finally, Fig. 13(c) shows RCS due to scattering from a PEC box of size $3\lambda \times 6\lambda \times 3\lambda$; meshed at three levels of discretization as shown in the inset figure. The discretizations are at $0.1\lambda, 0.2\lambda$, and 0.25λ. The RCS is computed using polynomials of orders $p = 1, 2, 3$ in each discretization range. This RCS is compared against one obtained using RWG basis
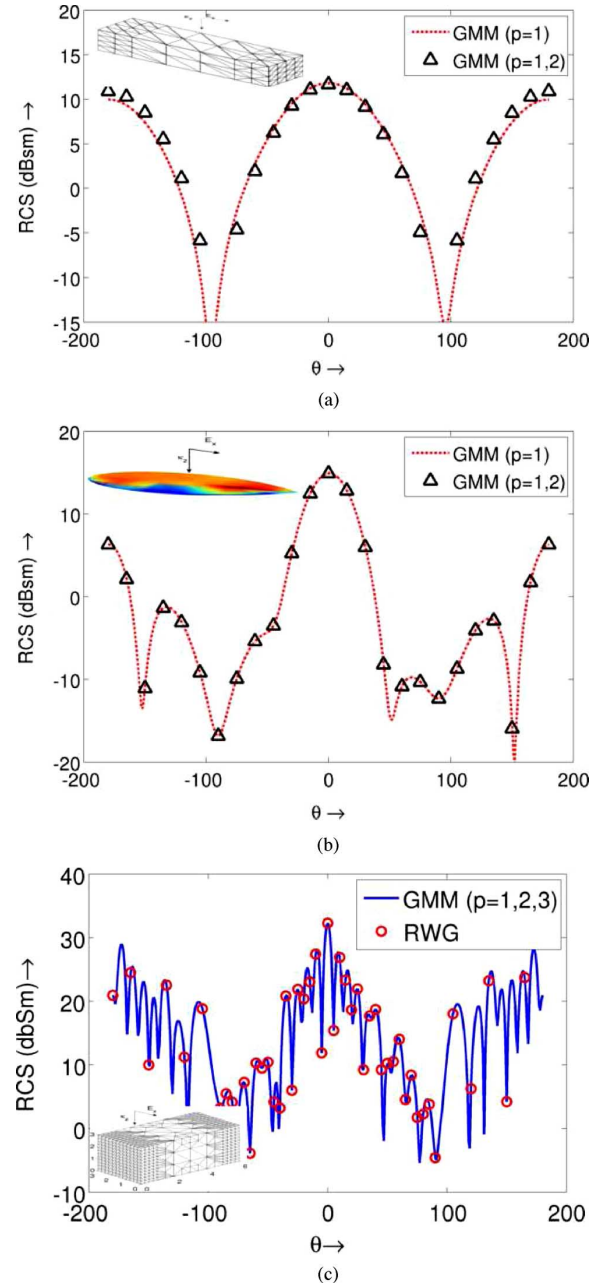

(a)

(b)

(c)

Fig. 13. RCS comparisons—mixed order GMM. (a) PEC box $(\lambda \times 4\lambda \times \lambda)$: GMM mixed order $(p = \{1, 2\})$ vs. standard GMM $p = 1$. (b) NASA Almond (1:3:9): GMM mixed order $(p = \{1, 2\})$ vs. standard GMM $p = 1$. (c) PEC Box $3\lambda \times 6\lambda \times 3\lambda$ GMM mixed order $(p = \{1, 2, 3\})$ vs. RWG $p = 1$.

functions on a uniform discretization of 0.1λ; and as can be seen from the figure, both results agree very well with each other.

2) Mixing Types of Basis Functions: The GMM scheme not only permits mixture of different orders of polynomial basis functions, but enables mixtures of different *types* of basis functions. As was mentioned earlier, the surface Helmholtz decomposition based system using scalar polynomial functions is only *one* possible way to define basis functions. In the following example, we demonstrate that these functions can be effortlessly combined with functions of the form $\hat{c} e^{i\mathbf{k} \cdot \mathbf{r}}$ where $\hat{c}$ is a pilot vector and $\mathbf{k}$ is the propagation vector.

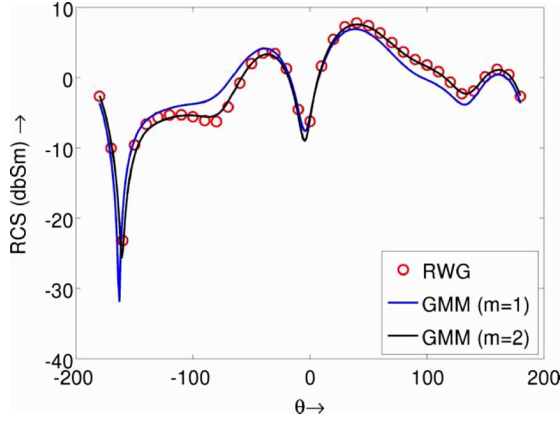Fig. 14. Box ($\lambda \times 0.5\lambda \times 0.5\lambda$): GMM with mixed basis functions (plane wave + polynomial) vs. standard polynomial GMM.

Consider scattering from a PEC box of size $\lambda \times 0.5\lambda \times 0.5\lambda$. The three sets of RCS data are compared in Fig. 14. One is obtained using GMM based polynomial basis functions of order $p = 1$ everywhere. The other two use a combination of polynomials of order $p = 1$ and plane-wave basis as described next. The plane wave basis functions used are defined as follows: $\boldsymbol{\nu}_i^m$ for patch Ω_i is defined as $\boldsymbol{\nu}_i^{m,1} = \hat{u}e^{i\mathbf{k}_m \cdot (\mathbf{r}-\mathbf{r}_i)}$ and $\boldsymbol{\nu}_i^{m,2} = \hat{v}e^{i\mathbf{k}_m \cdot (\mathbf{r}-\mathbf{r}_i)}$ where $\hat{u}$ and $\hat{v}$ are the local coordinate vectors, $\mathbf{r}_i$ is the center of patch i, and $\mathbf{k}_m$ is defined as $(\mathbf{k} \cdot \hat{u}) \cos(m\pi/(M+1))\hat{u} + (\mathbf{k} \cdot \hat{v}) \cos(m\pi/(M+1))\hat{v} \forall m \in \{0 \cdots M\}$. The three cases that are compared are as follows: (i) only polynomials, (ii) plane waves ($M = 1$) in all patches for $0.4\lambda \leq \hat{\mathbf{x}} \leq 0.6\lambda$ and polynomials elsewhere and finally (iii) using plane waves ($M = 2$) in patches $0.4\lambda \leq \hat{\mathbf{x}} \leq 0.6\lambda$ and polynomials elsewhere. A plane wave electric field polarized along $\hat{\mathbf{x}} - \hat{\mathbf{y}}$ is assumed incident along $\hat{\mathbf{x}} + \hat{\mathbf{y}}$ and the RCS is observed for all θ at $\phi = 0$. It is observed that as the number of plane wave is increased, the RCS obtained rapidly approaches that obtained using purely polynomials. This example illustrates that idea that not only can one used non-polynomial basis functions with ease within the GMM scheme but also use a combination of polynomial and non-polynomial basis functions.

3) Use of Non-Conformal Meshes: Finally, another advantage of the GMM arises from the initial motivation to separate the basis function definition from the tessellation of the geometry. Since, unlike the RWG, the GMM is not reliant on the tessellation; the GMM can be used with non-conformal meshes. It is common in practice to have different vendors mesh different areas of a geometry and this results in sets of meshes that need to be explicitly "stitched together" at the boundaries. There has been a considerable interest in the design of techniques that can handle non-conformal meshes [45]. However, a consequence of the design of the GMM scheme is that it can implicitly handle these kinds of meshes without any change to the framework or the implementation. Here we present one example illustrating this ability. Fig. 15(a) shows a $\lambda \times \lambda$ plate that is discretized at two slightly different scales; one at 0.1λ and the other at 0.15λ. These two halves are put together and a GMM covering is defined on this "non-conformal" tessellation. Fig. 15(b) shows the
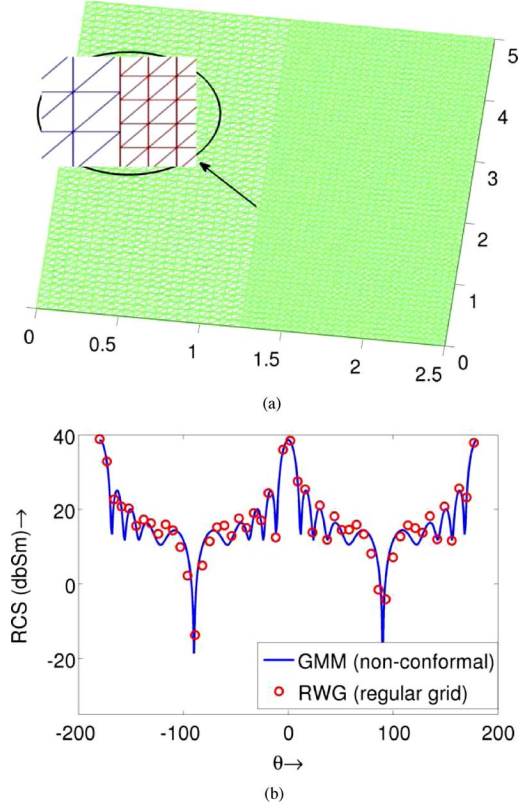

(a)

(b)

Fig. 15. Non Conformal meshes. (a) PEC plate ($\lambda \times \lambda$) discretized using two non-conformal meshes, (b) RCS comparison with standard RWG (on conformal mesh).

RCS obtained using the GMM scheme compared with the RCS obtained using a regular RWG discretization using a conformal meshing at 0.1λ of this plate.

D. Condition Number of the System

One of the consequences of using GMM is that the resultant discrete system appears to have a constant condition number over a wide range of frequencies. We have examined the condition number of the system over a wide range of frequencies for a variety of geometries. In each case, we use a constant mesh size that corresponds to an average edge length of 0.1λ at the highest frequency. This is used to construct the GMM patches (h varies from about 0.1λ to 0.4λ). The frequency is continuously reduced from 300 MHz to 3 Hz. The condition numbers of the impedance matrix obtained using regular RWG, GMM and loop-star basis functions are compared.

Fig. 16 shows the condition numbers for three geometries (i) PEC plate (size $1m \times 1m$, $N_{\text{GMM}} = 248$, $N_{\text{RWG}} = 228$) (ii) PEC cube (side $1m$, $N_{\text{GMM}} = 320$, $N_{\text{RWG}} = 1500$) and a sphere (0.2 m diameter, $N_{\text{GMM}} = 384$, $N_{\text{MoM}} = 480$). As expected, the regular MoM discretization is ill-conditioned at low frequencies. The loop-star scheme and the GMM scheme results in discrete systems with a constant condition number across a range of frequencies. It is evident from the figures that the condition number of the GMM scheme stays constant and is always less than or equal to the condition number of the loop-star scheme.
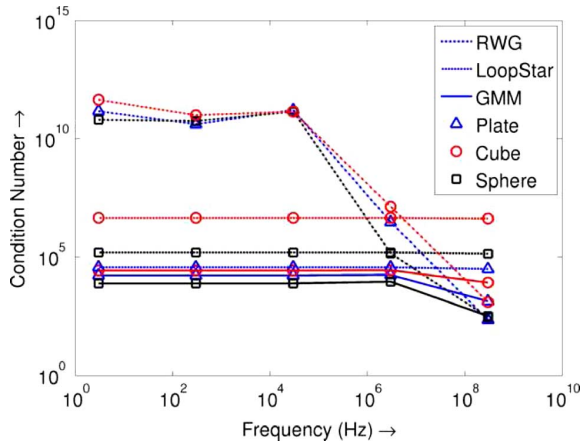
Fig. 16. EFIE Condition number comparisons for PEC sphere (0.2), square plate $(1m)$ and cube$(1m)$ using GMM, RWG and loop star basis.
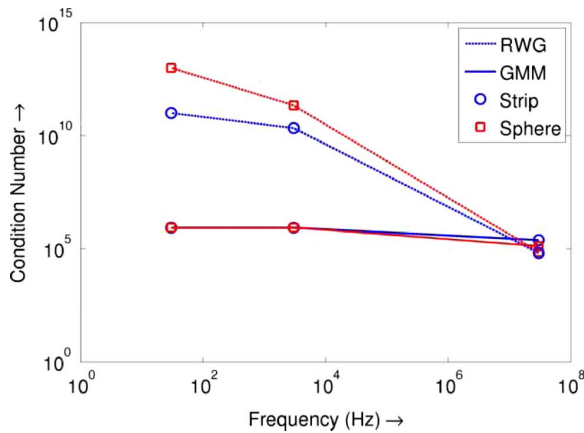

Fig. 18. EFIE Condition number comparisons for non-uniformly discretized square plate $(1m)$ and thin almond (1:3:9) using GMM and RWG and loop star basis.

Fig. 17. EFIE Condition number comparisons for PEC sphere $(0.2m)$ and strip $(1m \times 0.2m)$ using higher order $(p = 3)$ GMM and RWG basis.

Fig. 19. Comparison of RCS (GMM vs. loop star) at 30 MHz, 30 kHz and 3 kHz for constant h for a Plate: side $1m$.

The above results demonstrated condition number for discretization using linear basis functions. Fig. 17 shows the condition numbers obtained on discretizing using higher order basis functions for a 0.2 m diameter PEC sphere and PEC strip of dimensions $1m \times 0.2m$. The approximation functions used are third order complete and the condition numbers are compared against those obtained using a higher order RWG scheme using higher order RWG basis functions of the same order. Again, it is evident that the RWG condition number increases exponentially with frequency, whereas the GMM condition number remains constant.

The purpose of a low frequency stable system is the ability to handle meshes involving a large range of discretization sizes. To test the efficacy of the GMM scheme on such structures, we compare the GMM scheme with a standard RWG scheme on two geometries using multi-scale discretizations. Fig. 18 shows the variation of the condition number with frequency of the impedance matrix generated for a square PEC plate (side $1m$) and a thin almond of aspect ratio 1:3:9, both discretized non-uniformly. The ratio of the largest to smallest edge length used is 1:4 for the plate and 1:10 for the almond. The condition number is compared with both an RWG and a loop star scheme as the frequency is reduced. As can be clearly seen the condition number
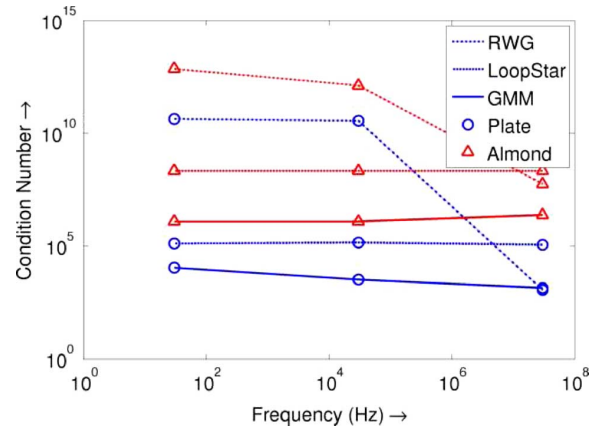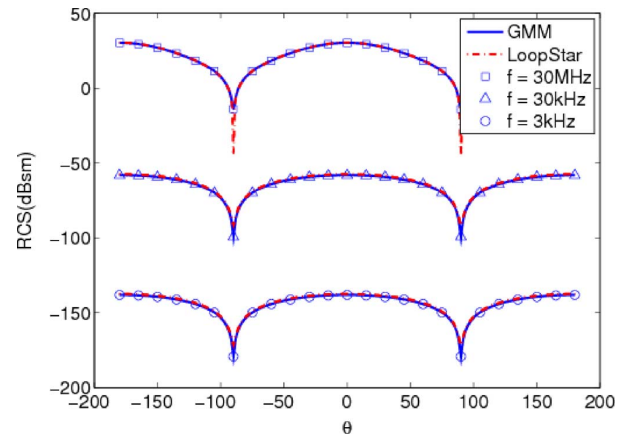
of the MoM scheme grows exponentially whereas the GMM condition number varies very slowly with frequency.

Finally, Fig. 19 shows the RCS for a square PEC plate (of side $1m$) obtained using the GMM and loop star basis functions. The figure shows the RCS at three different frequencies (30 MHz, 30 kHz and 3 kHz). The excellent agreement at all three frequencies demonstrate the low frequency *accuracy* of the proposed GMM scheme.

The variety of examples presented above demonstrate the ability of the GMM scheme coupled with the quasi-helmholtz basis functions to construct a well conditioned discretization scheme for the EFIE at low frequencies. While the full rationale for this behavior is still under investigation; the quasi-Helmtholtz nature of the basis functions is expected to be the major contributing factor to the well conditioned nature of the scheme. As an illustration of this idea; Fig. 20 shows the condition number obtained by using *only* the quasi-divergence free basis function for a PEC cube (of size 0.5 m) for a range of frequencies. As is clear from the figure; the condition number increases as the frequency is decreased; albeit at a much slower rate than for a standard RWG discretization. This points, indirectly, to the importance of the role played by the quasi-Helmholtz nature of the basis functions. However, it
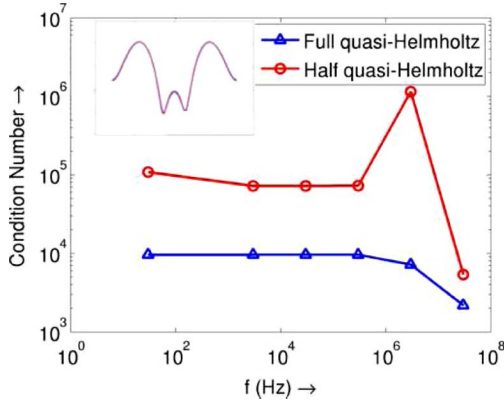
Fig. 20. Condition number vs. frequency for a PEC cube: comparison using one and two quasi-Helmholtz functions in approximation space.

should be pointed out that the GMM framework is crucial to the implementation of a locally quasi-Helmholtz basis function set and therefore; is critical to the well conditioned nature of the discretized integral equation.

VI. SUMMARY

In this work we have presented a framework for the discretization of electromagnetic integral equations that (i) provides considerable freedom over the choice of basis functions and (ii) eliminates the traditional coupling of the basis function and the discretization. Consequently, this provides a general structure wherein different basis functions can be seamlessly integrated to best approximate the currents locally. More importantly, it implies that it is not necessary to have basis functions that satisfy specific continuity requirements. As this is a departure from standard basis functions defined on tessellations, we have devised a methodology to use existing meshes to define basis functions and their domains of support. Results presented demonstrate the excellent approximation properties of the method as well as far field RCS data from three dimensional objects. Exemplary results have been presented to showcase several of the advantages of the GMM scheme. The results show that the scheme is low frequency stable, can handle mixture of types and orders of basis functions and that the mechanism is able to handle non conformal meshes.

APPENDIX

A transformation for the near singular integration of $\nabla g(R)\mathbf{j}(\mathbf{r}')$ for $\mathbf{r} \to \mathbf{r}'$. Consider the evaluation of the following integral for $\mathbf{r} \to \mathbf{r}'$ but $\mathbf{r} \neq \mathbf{r}'$:

$$\int_{\Delta}' d\mathbf{r}' \nabla g(R)\mathbf{j}(\mathbf{r}'). \tag{18}$$

We modify the steps outlined in [38] for the evaluation of

$$\int_{\Delta}' d\mathbf{r}' g(R)\mathbf{j}(\mathbf{r}'). \tag{19}$$

In [38], the authors split the triangle into three parts around the projection of $\mathbf{r}$ on to the tangent plane and use a geometric transformation to transform the integral to the following form:

$$\sum_{i=1}^{3} \int_0^{h_i} dy_i \int_{x_i(y_i)} dx_i \mathbf{j}(\mathbf{r}'(x_i, y_i))$$
$$\times e^{ikR} \frac{1}{\sqrt{(x_i^2 + y_i^2 + z^2)}} \tag{20}$$

where z is the height of the $\mathbf{r}$ above the equivalent tangent plane of the triangle Δ', h_i and x_i are the height and the base length of each sub triangle. [38] further uses an $\sinh^{-1}$ transformation to transfer the singularity of $1/\sqrt{x^2 + y^2 + z^2}$ from the integrand to the limits of the integral. It can be shown that a similar transfer of singularity can be achieved for $1/|\mathbf{r} - \mathbf{r}'|^2 = 1/x_i^2 + y_i^2 + z^2$ using a $\tan^{-1}$ transformation. The rest of the steps remain identical.

REFERENCES

[1] M. Andreasen, "Scattering from parallel metallic cylinders with arbitrary cross sections," *IEEE Trans. Antennas Propag.*, vol. 12, no. 6, pp. 746–754, Nov. 1964.

[2] J. Richmond, "Scattering by a dielectric cylinder of arbitrary cross section shape," *IEEE Trans. Antennas Propag.*, vol. 13, no. 3, pp. 334–341, May 1965.

[3] R. F. Harrington, *Time-Harmonic Electromagnetic Fields*, D. G. Dudley, Ed. Piscataway, NJ: IEEE Press, 2001.

[4] R. F. Harrington, *Field Computation by Moment Methods*. New York: IEEE Computer Society Press, 1993.

[5] J. Richmond, "Digital computer solutions of the rigorous equations for scattering problems," *Proc. IEEE*, vol. 53, no. 8, pp. 796–804, Aug. 1965.

[6] Y. Wang and H. Ling, "Radar signature prediction using method of moment codes via frequency extrapolation technique," *IEEE Trans. Antennas Propag.*, vol. 47, pp. 1008–1015, 1999.

[7] K. Zhao, M. Vouvakis, and J.-F. Lee, "The adaptive cross approximation algorithm for accelerated method of moments computations of EMC problems," *IEEE Trans. Electromagn. Compat.*, vol. 47, no. 4, pp. 763–773, Nov. 2005.

[8] G. Kobidze, J. Gao, B. Shanker, and E. Michielssen, "A fast time domain integral equation based scheme for analyzing scattering from dispersive objects," *IEEE Trans. Antennas Propag.*, vol. 53, no. 3, pp. 1215–1226, Mar. 2005.

[9] J. Nedelec, "Mixed finite elements in $\mathbb{R}^3$," *Numer. Math*, pp. 93–315, 1980.

[10] A. Bossavit and J.-C. Verite, "A mixed FEM-BIEM method to solve 3-D eddy-current problems," *IEEE Trans. Magn.*, vol. 18, no. 2, pp. 431–435, Mar. 1982.

[11] M. L. Barton and Z. J. Cendes, "New vector finite elements for three-dimensional magnetic field computation," *J. Appl. Phys.*, vol. 61, pp. 3919–3921, Apr. 1987.

[12] P.-A. Raviart and J. M. Thomas, *Mathematical Aspects of Finite Element Methods*. Berlin: Springer, 1975, vol. 606, ch. A mixed finite element method for 2nd order elliptic problems, pp. 292–315.

[13] S. M. Rao, D. R. Wilton, and A. W. Glisson, "Electromagnetic scattering by surfaces of arbitrary shape," *IEEE Trans. Antennas Propag.*, vol. 30, pp. 408–418, 1982.

[14] R. D. Graglia, D. R. Wilton, and A. F. Peterson, "Higher order interpolatory vector bases for computational electromagnetics," *IEEE Trans. Antennas Propag.*, vol. 45, pp. 329–342, 1997.

[15] W. Cai, T. Yu, H. Wang, and Y. Yu, "High-order mixed RWG basis functions for electromagnetic applications," *IEEE Trans. Microw. Theory Tech.*, vol. 49, no. 7, pp. 1295–1303, July 2001.

[16] A. F. Peterson and M. M. Bibby, "High-order numerical solutions of the MFIE for the linear dipole," *IEEE Trans. Antennas Propag.*, vol. 52, pp. 2684–2691, 2004.

[17] M. M. Bibby, A. F. Peterson, and C. M. Coldwell, "High order representations for singular currents at corners," *IEEE Trans. Antennas Propag.*, vol. 56, pp. 2277–2287, 2008.

[18] N. Nair, C. Lu, and B. Shanker, "Differential and integral equation solvers based on generalized moments and partitions of unity," in *Proc. Int. Conf. on Electromagnetics in Advanced Applications*, Sep. 2007, pp. 974–977.

[19] D. Wilton and S. Govind, "Incorporation of edge conditions in moment method solutions," *IEEE Trans. Antennas Propag.*, vol. 25, no. 6, pp. 845–850, Nov. 1977.

[20] W. Brown and D. Wilton, "Singular basis functions and curvilinear triangles in the solution of the electric field integral equation," *IEEE Trans. Antennas Propag.*, vol. 47, no. 2, pp. 347–353, Feb. 1999.

[21] R. Graglia and G. Lombardi, "Singular higher order complete vector bases for finite methods," *IEEE Trans. Antennas Propag.*, vol. 52, no. 7, pp. 1672–1685, July 2004.

[22] J. M. Melenk and I. Babuska, "The partition of unity finite element method: Basic theory and applications," *Comput. Methods Appl. Mechan. Eng.*, vol. 139, pp. 289–314, 1996.

[23] C. Lu and B. Shanker, "Generalized finite element method for vector electromagnetic problems," *IEEE Trans. Antennas Propag.*, vol. 55, no. 5, pp. 1369–1381, May 2007.

[24] G. Hsiao and R. Kleinman, "Mathematical foundations for error estimation in numerical solutions of integral equations in electromagnetics," *IEEE Trans. Antennas Propag.*, vol. 45, no. 3, pp. 316–328, Mar. 1997.

[25] I. Babuska and J. M. Melenek, "The partition of unity method," *Int. J. Numer. Methods Engrg.*, vol. 40, pp. 727–858, 1997.

[26] O. Tuncer, C. Lu, N. V. Nair, B. Shanker, and L. C. Kempel, "Further development of vector generalized finite element method and its hybridization with boundary integrals," *IEEE Trans. Antennas Propag.*, vol. 58, no. 3, pp. 887–899, 2010.

[27] E. M. Hyde, "Fast, High-Order Methods for Scattering by Inhomogenous Media," Ph.D. dissertation, California Inst. Technol., Pasadena, 2003.

[28] O. P. Bruno, "Fast, high-oder, high-frequency integral methods for computational acoustics and electromagnetics," in *Topics in Computational Wave Propogation: Direct and Inverse Problems*, ser. Lecture Notes in Computational Science and Engineering. Berlin: Springer, 2003, pp. 43–82, no. 31.

[29] O. P. Bruno and L. A. Kunyansky, "Surface scattering in three dimensions: An accelerated high-order solver," in *Proce. Royal Society A: Math., Phys. Engrg. Sci.*, 2001, vol. 457, pp. 2921–2934.

[30] O. P. Bruno and L. A. Kunyansky, "A high-order algorithm for the solution of surface scattering problems: Basic implementation, tests and applications," *J. Comput. Phys.*, vol. 169, pp. 80–110, 2001.

[31] L. A. Kunyansky and O. P. Bruno, "A fast, high-order algorithm for the solution of surface scattering problems II: Theoretical considerations," *J. Comput.l Phys.*, vol. 169, pp. 80–110, 2001.

[32] R. Scharstein, "Helmholtz decomposition of surface electric current in electromagnetic scattering problems," in *Proc. 23rd Southeastern Symp. on System Theory, 1991*, Mar. 1991, pp. 424–426.

[33] N. Nair, B. Shanker, and L. Kempel, "Generalized Method of Moments: A Novel Discretization Technique for Integral Equations," Tech. Rep., Michigan State University, 2010.

[34] A. Buffa and S. H. Christiansen, "A dual finite element complex on the barycentric refinement," *Math. Comput.*, vol. 76, no. 260, pp. 1743–1769, 2007.

[35] C. Delgado, E. Garcia, F. Catedra, and R. Mittra, "Generation of characteristic basis functions defined over large surfaces by using a multilevel approach," *IEEE Trans. Antennas Propag.*, vol. 57, no. 4, pp. 1299–1301, Apr. 2009.

[36] L. Knockaert, "A general Gauss theorem for evaluating singular integrals over polyhedral domains," *Electromagnetics*, pp. 269–280, 1991.

[37] S. Jarvenpaa, M. Taskinen, and P. Ylä-oijala, "Singularity extraction technique for integral equation methods with higher order basis functions on plane triangles and tetrahedra," *Int. J. Numer. Methods Engrg.*, vol. 58, pp. 1149–1165, 2003.

[38] M. Khayat and D. Wilton, "Numerical evaluation of singular and near-singular potential integrals," *IEEE Trans. Antennas Propag.*, vol. 53, no. 10, pp. 3180–3190, Oct. 2005.

[39] T. Terai, "On calculation of sound fields around three dimensional objects by integral equation methods," *J. Sound Vibrat.*, vol. 69, pp. 71–100, 1980.

[40] L. F. Canino, J. J. Ottusch, M. A. Stalzer, J. L. Visher, and S. M. Wandzura, "Numerical solution of the Helmholtz equation in 2D and 3D using a high-order Nystrom discretization," *J. Comput. Phys.*, vol. 146, no. 2, pp. 627–663, 1998.

[41] R. Coifman, V. Rokhlin, and S. Wandzura, "The fast multipole method for the wave equation: A pedestrian prescription," *IEEE Antennas Propag. Mag.*, vol. 35, no. 3, pp. 7–12, 1993.

[42] M. Vikram and B. Shanker, "An incomplete review of fast multipole methods from static to wideband as applied to problems in computational electromagnetics," *Appl. Computat. Electromagn. Society J.*, vol. 27, p. 79, 2009.

[43] M. Vikram, H. Huang, B. Shanker, and T. Van, "A novel wideband fmm for fast integral equation solution of multiscale problems in electromagnetics," *IEEE Trans. Antennas Propag.*, vol. 57, no. 7, pp. 2094–2104, Jul. 2009.

[44] A. Chatterjee, J. Jin, and J. L. Volakis, "Edge-based finite elements and vector ABC's applied to 3-D scattering," *IEEE Trans. Antennas Propag.*, vol. 41, pp. 221–226, 1993.

[45] M. Vouvakis, K. Zhao, S.-M. Seo, and J.-F. Lee, "A domain decomposition approach for non-conformal couplings between finite and boundary elements for unbounded electromagnetic problems in," *J. Comput. Phys.*, vol. 225, no. 1, pp. 975–994, 2007.

Naveen V. Nair (S'03) received the B.Tech. and M.Tech. degrees in mechanical engineering from the Indian Institute of Technology, Madras, India, in 2003. He defended his Ph.D. thesis from Michigan State University in 2010.

He is currently employed as a Visiting Research Associate in Computational Electromagnetics Laboratory, Michigan State University, East Lansing. His research interests include computational and numerical techniques with specific applications to electromagnetics, inverse problems and nondestructive evaluation.

Balasubramaniam Shanker (SM'03-F'09) received the B.Tech. degree from the Indian Institute of Technology, Madras, India, in 1989, and the M.S. and Ph.D. degrees from the Pennsylvania State University, University Park, in 1992 and 1993, respectively.

From 1993 to 1996, he was a Research Associate in the Department of Biochemistry and Biophysics, Iowa State University, where he worked on the Molecular Theory of Optical Activity. From 1996 to 1999, he was with the Center for Computational Electromagnetics, University of Illinois at Urbana-Champaign, as a Visiting Assistant Professor, and from 1999–2002 with the Department of Electrical and Computer Engineering, Iowa State University, as an Assistant Professor. Currently, he is an Professor in the Department of Electrical and Computer Engineering, Michigan State University. He has authored/coauthored over 300 journal and conferences papers and presented a number of invited talks. His research interest include all aspects of computational electromagnetics (frequency and time domain integral equation based methods, multi-scale fast multipole methods, fast transient methods, higher order finite element and integral equation methods), propagation in complex media, mesoscale electromagnetics, and particle and molecular dynamics as applied to multiphysics and multiscale problems.

Prof. Shanker is a Fellow of IEEE, elected for his contributions in computational electromagnetics, and is a full member of the USNC-URSI Commission B. He was awarded the Withrow Distinguished Junior scholar (in 2003), the Withrow teaching award (in 2007) and the Withrow Distinguished Senior scholar (in 2010). He was an Associate Editor for the IEEE ANTENNAS AND WIRELESS PROPAGATION LETTERS (AWPL) and is currently an Associate Editor for the IEEE TRANSACTIONS ON ANTENNAS AND PROPAGATION.